ADVANCED OPTICAL MATERIALS
www.advopticalmat.de

Toward Direct Laser Writing of Dual-Layer Metasurfaces with the Plasmonic Phase-Change Material In_3SbTe_2

Lukas Conrads, Maike Kreutz, Lina Jäckering, Sebastian Meyer, Matthias Wuttig, Dmitry Chigrin, and Thomas Taubner**

Metasurfaces have emerged as a versatile tool for tailoring light-matter interaction. Combining multiple metasurfaces and antenna arrays in a multi-layer structure promises intrinsic chiral structures as well as circumventing conventional metasurface drawbacks such as chromatic aberrations. For non-volatile metasurface tuning, phase-change materials (PCMs) have evolved as prime candidates. Recently, the plasmonic PCM In_3SbTe_2 (IST) has been established which can be reversibly switched from an amorphous dielectric to a crystalline metallic state in the infrared via laser irradiation. While optically reconfiguring antenna shapes with IST has been extensively studied in a single layer structure, fabrication of a multi-layer IST metasurface for individual resonance control in the different layers has not been shown yet. Here, a proof-of-concept of individual resonance control is shown in a dual-layer IST metasurface with precise laser pulses from the top and from the bottom through the substrate. The complex switching dynamics and temperature distribution with Multiphysics simulations are theoretically explored. Subsequently, two antenna structures in both layers for multiple polarization dependent resonances are investigated. Finally, chiral meta-atoms are combined as possible applications for dual-layer IST metasurfaces. A wide range of applications is envisioned for dual-layer metasurfaces by rapid prototyping chiral and reconfigurable antenna structures.

1. Introduction

Metasurfaces facilitate miniaturization of optical components with the ability to realize intriguing and unconventional physical phenomena. In general, metasurfaces are composed of subwavelength nanostructures arranged on a 2d plane in order to tailor the amplitude, phase, and polarization of the scattered light.[1]

Nowadays, metasurfaces are employed in many different areas as a planar platform for, e.g., lensing,[2] beam steering,[3] color filters,[4] and holography.[5]

While the most basic metasurfaces conventionally feature only a single functionality, multifunctional optical devices are strongly demanded for pushing the limits of integrated photonics and real-world applications.[6] Several approaches have been explored ranging from stacking metasurfaces with single functionalities to encoding multiple functionalities within the same metasurface for 2 beam steering or holography.[7–9]

Chiral metasurfaces are characterized by intrinsic or extrinsic chirality. Extrinsic chirality is achieved by breaking the symmetry with oblique incidence to create a chiral response. In contrast, intrinsic chirality is given if the structure itself lacks mirror symmetry and is independent from the illumination direction.[10] Chiral metasurfaces enable different responses of the chiral structures dependent on the spin of the incident photons.[10–13] Consequently, numerous applications such as chiral sensing,[14] spin-selective frequency conversion[15] and holography[16] have been studied.

However, these complex, nearly 3d metasurfaces are usually static, e.g., post-fabrication adaptations and dynamic tuning are not possible.

For non-volatile resonance tuning phase-change materials have been evolved as prime candidates because of their two (meta-)stable phases which differ significantly in their electrical and optical properties.[17,18] The reason for the tremendous contrast of both phases relies on the chemical bonding. Upon phase change, the covalently bonded atoms in the amorphous phase become metavalently bonded in the crystalline phase.[19–23] Reversible switching between those two phases is achieved with electrical or optical pulses. Several applications for nanophotonic components have been realized in the previous years, ranging from tunable lenses,[24] absorbers,[25–27] beam steering devices,[28,29] spatial light modulators[30] to tunable chiral metasurfaces.[31,32]

Conventionally, switching the phase-change material results in a contrast in the dielectric function modifying the dielectric environment of the nanoantennas.[33,34] While In_3SbTe_2 (IST) was

L. Conrads, M. Kreutz, L. Jäckering, S. Meyer, M. Wuttig, D. Chigrin, T. Taubner
Institute of Physics (IA)
RWTH Aachen University
D-52056 Aachen, Germany
E-mail: conrads@physik.rwth-aachen.de; taubner@physik.rwth-aachen.de

The ORCID identification number(s) for the author(s) of this article can be found under https://doi.org/10.1002/adom.202500215

DOI: 10.1002/adom.202500215

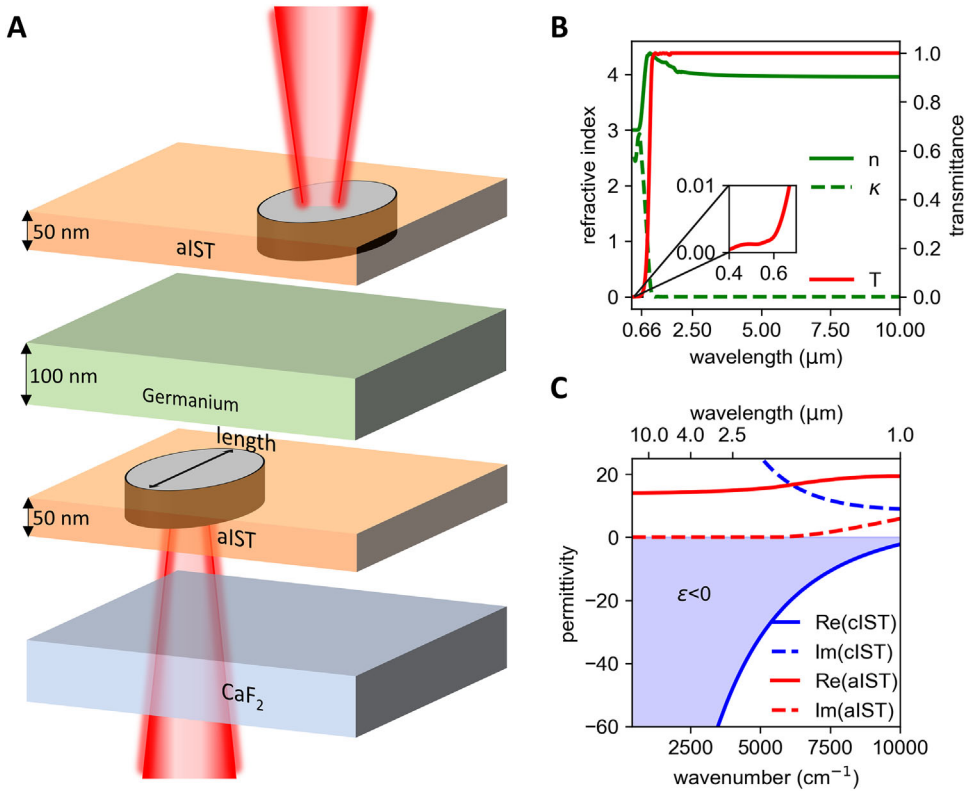

Figure 1. Design idea of optically programming dual-layer IST metasurfaces. A) Schematic sketch of the dual-layer IST sample separated by a germanium layer. Our core idea is to obtain crystallization (gray ellipses) of the upper (lower) layer with precise laser pulses from the top (bottom through the substrate). B) Real and imaginary part of the refractive index of germanium. While germanium is opaque in the visible, it is completely transparent in the infrared. C) Real and imaginary part of the permittivity of IST. Upon crystallization, the real part of the permittivity becomes negative and shows a Drude-like behavior.

originally explored for data storage technology,[35] Heßler et al. recently introduced IST as a plasmonic PCM into nanophotonics which can be switched from an amorphous dielectric phase to a crystalline metallic one in the entire infrared spectral range.[36] Hence, by locally crystallizing IST, plasmonic nanoantennas can be directly written and reconfigured within the amorphous dielectric surrounding. Not only reconfiguring of electric[36,37] and magnetic[38,39] dipole resonances as well as large area emissivity shaping metasurfaces[40–42] have been successfully demonstrated, but also modifying polaritons[43–45] and infrared beam shaping[46] with geometric phase metasurfaces. However, the experiments demonstrated focused only on optically programming of single layer metasurfaces without direct fabrication of multiple cascaded metasurfaces or antenna arrays, hence preventing, e.g., tailored intrinsic chirality with IST.

Here, we investigate a dual-layer IST metasurface separated by a thin dielectric layer. The core idea is to individually address the different IST layers with precise laser pulses allowing for independent control of the crystallization in both layers. With the help of Multiphysics simulations, we reveal the temperature distribution within the layers upon laser irradiation from the top and the bottom of the layer stack. We fabricate antenna structures in the individual layers via laser crystallization and reamorphization from the top and through the substrate and experimentally investigate the antenna resonances. Afterward, we experimentally study rotated antennas in both layers for multiple polarization dependent resonances. Finally, we theoretically analyze the intrinsic chirality of the designed metasurface.

2. Main Text

The investigated layer stack (see **Figure 1A**) consists of an infrared transparent CaF_2 substrate with a 50 nm thin amorphous IST layer on top. A second 50 nm amorphous IST layer is separated by a 100 nm thin germanium layer to enable programming of antenna structures in different layers. On top, a 70 nm thin $ZnS:SiO_2$ capping layer is employed (omitted in the sketch for better visibility). In particular, the germanium layer is opaque for visible light with 0.9% transmittance (and around 50% reflectance) at the 660 nm employed switching wavelength and transparent in the entire infrared spectral range with a constant refractive index ≈4.[47] (c.f. Figure 1B). The idea is to tailor the switching process via laser irradiation either from the top to crystallize the upper IST layer, or from the bottom through the substrate to crystallize the lower IST layer. The germanium spacer layer serves mainly as barrier for visible light to distinguish the optically written antennas in the different layers and not for controlling the absorption of the switching laser across the layers. Upon crystallization, the real part of the permittivity changes from a positive value in the amorphous phase to a negative one

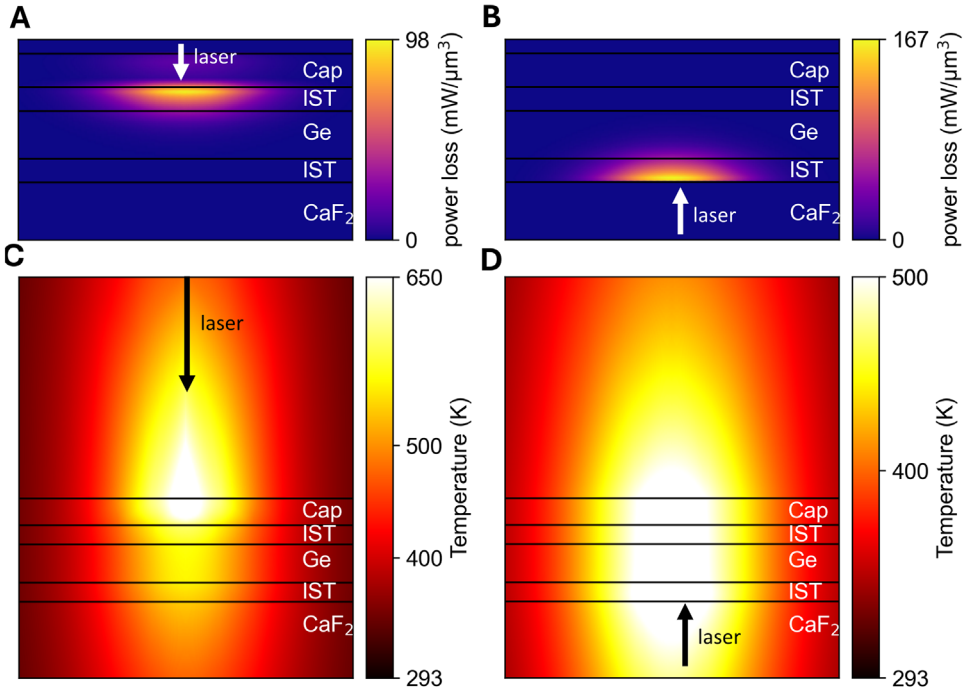

Figure 2. Field simulations optical switching. A,B) Simulated power losses within the layer stack for laser illumination from the top (A) and through the substrate (B). The absorption mainly takes place in the IST which is penetrated by the laser first. C,D) Simulated temperature distribution after 800 ns within the layers for different illumination directions. If the sample is illuminated from the top (C), the heat is mainly confined within the upper layer. The temperature in the upper layer is 50 K larger compared to the lower layer. In contrast, for the illumination from the bottom (D), a homogeneous temperature distribution across the layers is obtained.

in the crystalline phase (c.f. Figure 1C). In the infrared, the complex permittivity of crystalline IST follows a Drude-like behavior with the plasma frequency located at 900 nm. More details about the permittivity of IST are found in ref. [36].

We first perform multiphysics simulations to gain a better understanding of the corresponding crystallization dynamics upon laser irradiation by simulating the laser absorption for switching from the top and the bottom through the substrate.[48,49] The absorbed power upon laser irradiation is transferred into the temperature distribution across the layer stack. First, the electromagnetic losses upon laser irradiation with a wavelength of 660 nm are simulated for illumination from the top and the bottom in **Figure** 2A,B in the x-z cross section. Detailed information about the thermal simulations can be found in the Experimental Section. For both illumination directions, the absorption mainly takes place within the IST layers which is first penetrated by the laser. The remaining layers feature almost no absorption, indicating that the entire laser power is confined and subsequently converted into heat within the respective IST layers. In general, this might lead to the conclusion that switching IST in the individual layers is easily possible. However, converting the simulated power losses into heat within the system yields a more complex temperature distribution than initially expected. The corresponding temperature maps of the layer stack 800 ns after irradiation are displayed in Figure 2C,D. If the sample is illuminated from the top (c.f. Figure 2C), the strongest temperature increase is revealed at the interface of the sample with air due to the low thermal conductivity of air. Consequently, the heat is mainly confined to the upper IST layer because the heat conductivity within the different layers and especially of the substrate compared to air leads to smaller temperatures in the lower layers. If the sample is illuminated from the bottom through the substrate (c.f. Figure 2D), a more homogeneous temperature distribution is visible across the different layers. This phenomenon is caused by the larger thermal conductivities of the layers compared to air. Accordingly, both IST layers will crystallize for laser irradiation from below, while laser irradiation from above will only yield crystallization in the upper IST layer. Even a spacer layer of SiO_2 with a much smaller thermal conductivity leads to similar temperature pattern (see Note S1, Supporting Information). Increasing the germanium layer thickness might lead to stronger temperature differences in both layers, but would also decrease the antenna coupling.

Consequently, we have to develop an experimental strategy to overcome the crystallization in both IST layers by applying a subsequent reamorphization step of antennas in the upper layer, leading to antennas only present in the lower layer.

First, we experimentally investigate the antenna resonances only in a single layer. Antenna arrays consisting of 5×5 antennas with a period of 3.3 µm in x- and y-direction in the upper layer are crystallized with elliptically shaped laser spots (see Experimental Section for details) with a power of 1.93 mW and 250 ns pulse duration from the top (c.f. schematic sketch in **Figure** 3A). The resulting antenna length in y-direction and width in x-direction are determined to 1.3 and 1 µm, respectively. Afterward, the antenna length is increased up to 2.6 µm by applying vertically shifted crystallization spots at the antenna ends to reconfigure the once written antenna arrays. Light microscope images of the

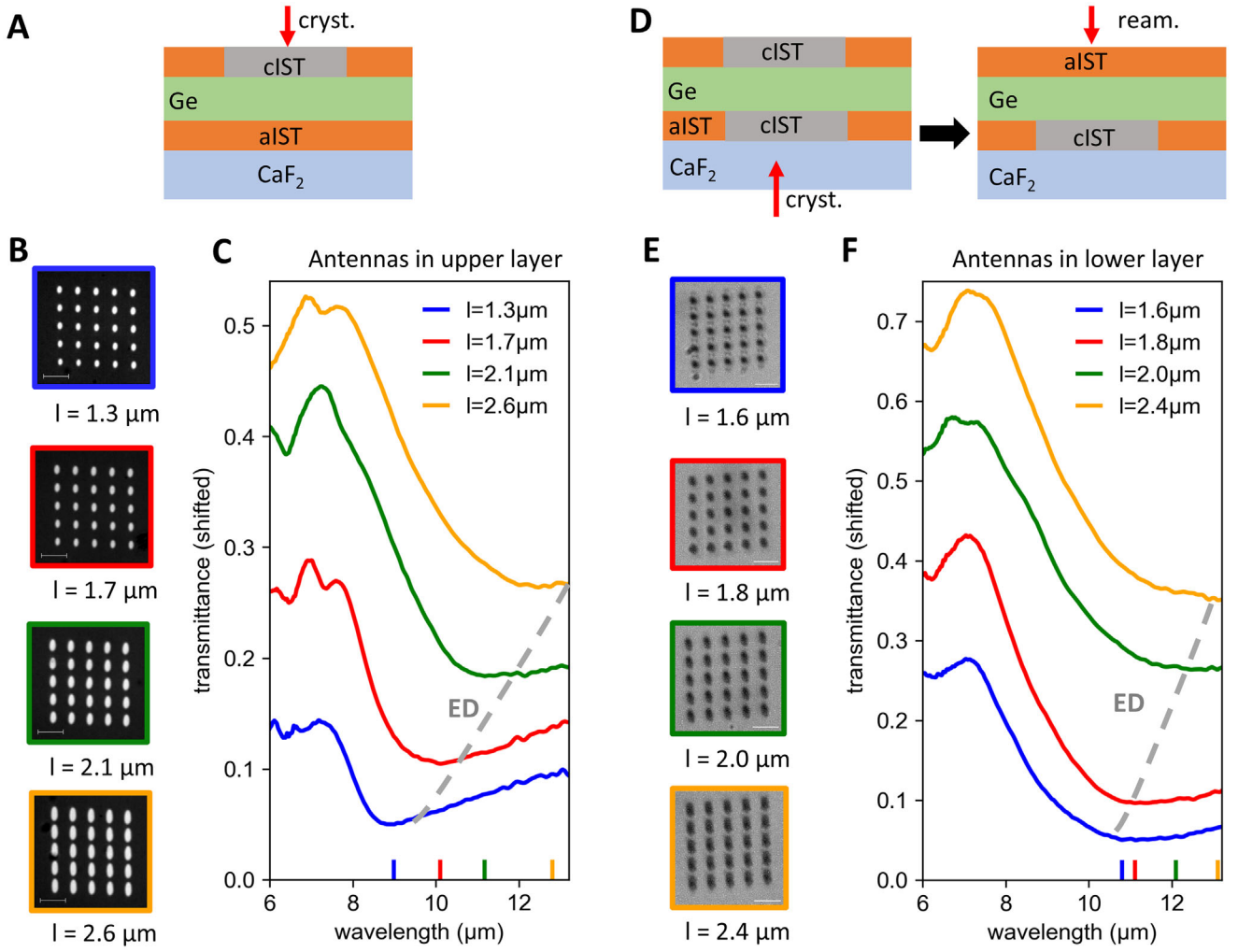

Figure 3. Investigation of antennas in single layers only. A) Schematic sketch of optically crystallizing antennas in the upper layer via laser irradiation from the top. B) Light microscope images (reflection) of crystalline IST antennas in the upper layer. Vertically shifting multiple crystallization pulses results in reconfigured antennas with lengths ranging from 1.3 to 2.6 µm. C) Measured transmittance spectra of the arrays shown in (B). The shift of the electric dipole (ED) resonance is highlighted with the gray dashed line. D) Schematic sketch of crystallizing antennas in both layers through the substrate with a second erasing step of the antennas in the upper layer. E) Light microscope images (transmission) of antennas with increased lengths in the lower IST layer. F) Measured transmittance spectra of the antenna arrays from E. The gray line is a guide-to-the-eye for the ED resonance. The scale bars in the microscope images equal 5 µm.

fabricated arrays in reflectance mode are shown in Figure 3B. The transmittance spectra are measured via Fourier transform infrared (FTIR) spectroscopy with vertically polarized light (see Experimental Section) and displayed in Figure 3C. The blue curve corresponding to antennas with a length of 1.3 µm exhibits a minimum at 8.5 µm associated with the electric dipole resonance. Upon increasing the antenna length, the electric dipole resonance shifts toward larger wavelengths. The results are consistent with previous experiments shown in literature considering only a single IST layer on top of a substrate.[36]

To crystallize antennas in the lower layer, the sample is turned upside down and the PCM is switched through the substrate (c.f. Figure 3D). Now, larger laser switching powers are required due to the reflection at the boundary between air and the substrate. In particular, the laser power and pulse duration are increased to 17.47 mW and 400 ns, respectively. Again, we apply vertically shifted crystallization pulses to tune the antenna length. As already explained in Figure 2D, the temperature distribution across the different layers is approximately homogeneous, leading to crystallization in both layers. Measured transmittance spectra and numerical simulations of antennas in both layers can be found in Note S2 (Supporting Information). Afterward, the crystallized spots in the upper layer are reamorphized from the top with single laser shots with 110.3 mW and 21 ns pulse duration to erase antennas in the upper layer and ensure antennas only in the lower layer (c.f. schematic sketch in Figure 3D). Transmission light microscope images are shown in Figure 3E. Because these images are recorded in transmission mode, the crystallized antennas appear black (light cannot be transmitted) compared to the bright area representing the amorphous surrounding. Here, the antenna length is varied from 1.6 to 2.4 µm. Light microscope images in reflection mode verifying that the upper layer is

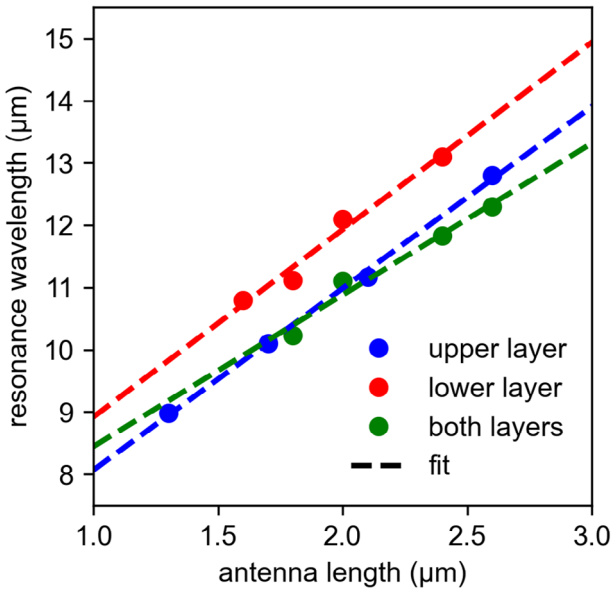

Figure 4. Resonance wavelengths of antennas in the different layers. The resonance wavelengths for different antenna lengths in the lower layer (red dots), the upper layer (blue dots), and both layers (green dots) are obtained from the experimental data. The dashed line represents a linear fit.

fully amorphous are shown in Supplementary Note S3 (Supporting Information). The measured transmittance spectra of those antenna arrays (c.f. Figure 3F) exhibit electric dipole resonances shifted from 10.8 µm for antennas with a length of 1.6 to 13.4 µm for antennas with a length of 2.4 µm. Numerical simulations for antennas of varied length in the different layers can be found in Note S4 (Supporting Information) and are in good agreement with the experimentally obtained spectra.

In general, the resonance wavelength of simple rod antennas scales linearly with the antenna length. The experimentally obtained resonance wavelengths for antennas in the upper, lower, and both layers for increasing antenna lengths are shown in **Figure 4**. The larger resonance wavelength for antennas in the lower layer compared to antennas of similar sizes in the upper layer is caused by the larger refractive index of the substrate compared to air in closer vicinity of those antennas. If antennas in both layers are present, the transverse coupling of both parallel oriented dipoles leads to a resonance blue-shift compared to antennas in the individual layers.[50]

Therefore, we are able to individually program antenna arrays in the upper and the lower layer via laser irradiation either from the top, or from the bottom through the substrate by erasing the crystallized spots in the upper layer. The ability to reconfigure and even erase once written structures highlights the tremendous flexibility of IST as a programmable nanophotonic platform.

In the next step, the infrared response of antenna arrays vertically stacked in both layers are experimentally investigated. Since the measured and simulated spectra of antennas with the same orientation in both layers prevent a clear distinction between the individual contribution of the different antennas (see Note S2, Supporting Information), we exploit the polarization-dependent response of two antennas rotated by 90° with respect to each other. These antennas are optically programmed in the lower and upper layer with the previously explained writing and erasing procedure. In particular, antennas in the lower layer are oriented in x-direction, while antennas in the upper layer are oriented in y-direction. An exemplary scattering-type scanning near-field optical microscopy[51] image of these antennas can be found in Note S5 (Supporting Information). There, we exploit the subsurface imaging capabilities of s-SNOM[52,53] to image IST antennas even buried below 220 nm of other materials, validating the presence of antennas in the individual layers. Reflectance light microscope images of the upper layer are shown in **Figure 5**A in comparison with a transmittance image of the antennas in the lower layer (black frame). The size of the antennas in the upper layer is varied by crystallizing the upper layer with 2.7 mW and pulse durations varied from 200 to 400 ns, leading to antenna lengths $l_{1,y}$ varying from 1.4 to 2.0 µm. Notice, that due to the elliptically shaped laser spot the antenna width increases too from 1 to 1.5 µm. In the lower layer, the long axis of the antennas is horizontally oriented with a length $l_{2,x} = 2.2$ µm.

The measured transmittance spectra for polarized light in x- and y-direction are displayed in Figure 5B. The electric dipole resonances for the horizontally oriented antennas in the lower layer excited with polarized light in x-direction remain at the same wavelength of ≈12 µm (dotted lines). In contrast, if the antenna arrays are illuminated with light polarized in y-direction, the electric dipole resonance shifts toward larger wavelengths for larger antenna lengths (solid lines). The experimentally obtained results are supported by numerical simulations in Figure 5C showing the same trend. In particular, the obtained resonance wavelengths match well and even smaller features such as the shoulder at approx. 7.5 µm are reproduced. The pronounced maximum in the transmittance spectra at 6.5 µm is caused by grating resonances which are dampened in the experimental spectra due to the usage of Cassegrain objectives featuring multiple angles of incidence.[54]

Finally, numerical field simulations are performed in Figure 5D,E to validate the origin of the resonance modes occurring in the measured and simulated spectra. Accordingly, the electric fields of antennas in the upper layer with a length of 1.4 µm and antennas in the lower layer with a length of 2.2 µm are examined (see red spectra in Figure 5C) for both layers. The electric field patterns of the antennas for polarized light in y-direction with a wavelength of 12 µm reveal strong field enhancement of the antenna in the lower layer at the long antenna axis. The smaller antenna in the upper layer displays only moderate field enhancement at the short axis, validating the assignment of this resonance to the antennas in the lower layer. In contrast, at a wavelength of 10 µm (see Figure 5E), the smaller antenna in the upper layer displays stronger fields parallel to the antenna axis. The coupling of the antennas with varying positions and orientations, e.g. for creation of intrinsic chiral structures, is a topic of future investigations.

Consequently, we are able to optically program nanoantennas of varied antenna length independently in both layers in only three optical writing steps, i.e., first crystallization and second subsequent reamorphization and new crystallization of the upper layer, without performing multiple etching and mask design processes (see Note S6, Supporting Information for a comparison with conventional fabrication).

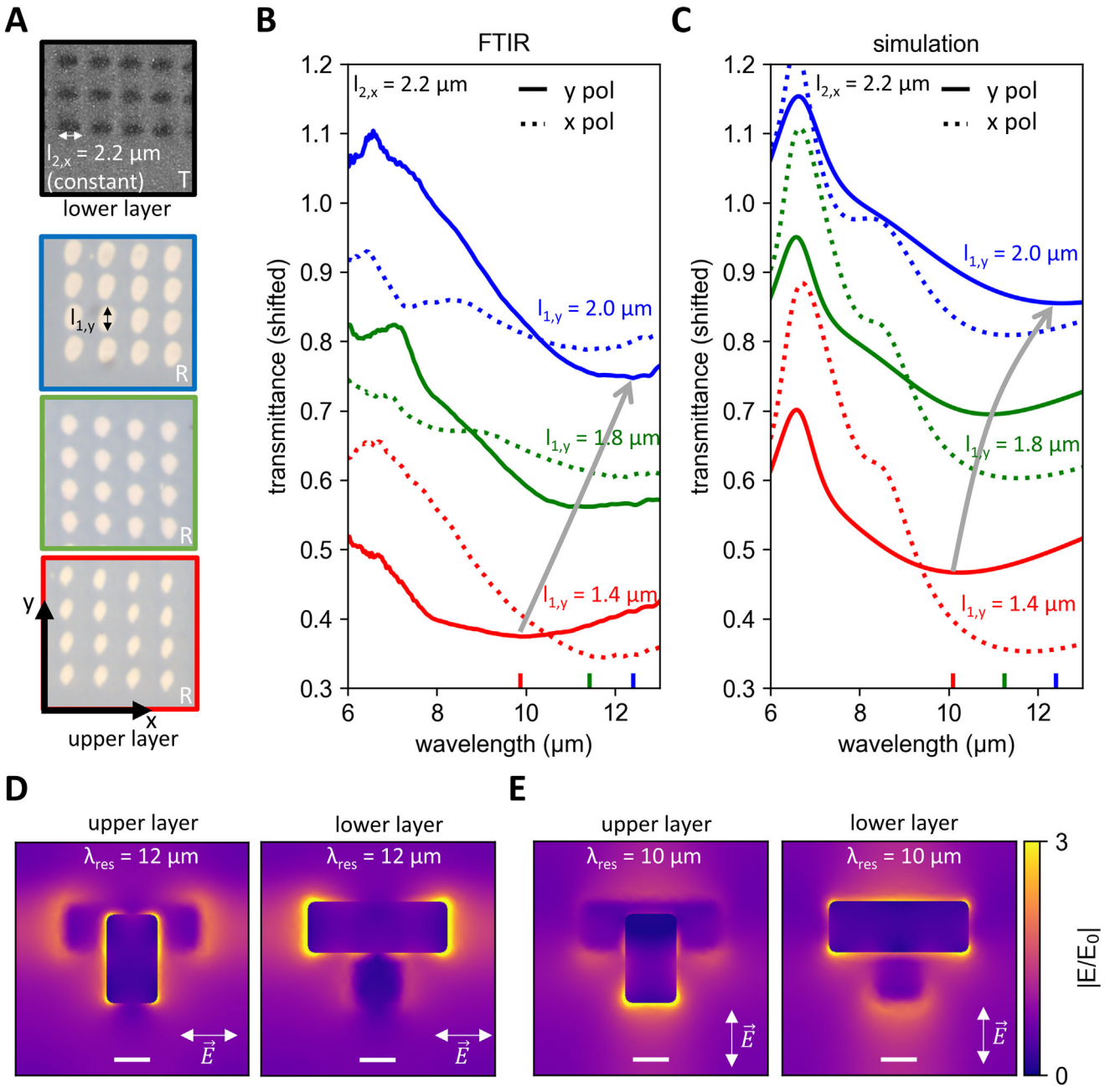

Figure 5. Rotated antennas in both layers. A) Light microscope images of the fabricated antennas. The upper image (black frame) recorded in transmission mode displays the antennas in the lower layer (oriented along the x-axis). The images with colored frames show reflectance images of the antennas in the upper layer (oriented along the y-axis). B) Measured and simulated (C) transmittance spectra for light polarized in y-direction (solid) and x-direction (dashed) for varied antenna lengths in the upper layer. D) Electric field simulations at 12 µm for light polarized in x-direction. The larger antenna in the lower layer displays enhanced fields at the end. E) Electric field simulations at 10 µm for light polarized in y-direction. Now, the smaller antenna in the lower layer shows an electric dipole resonance. The scale bars are 500 nm.

Finally, we investigate an intrinsically chiral metasurface with numerical simulations. As stated before, chiral metasurfaces can consist of intrinsic or extrinsic chiral structures. For example, L-shaped antennas are extrinsically chiral because a mirror symmetry along the diagonal can be achieved. While the antenna itself might possess mirror symmetry, breaking this symmetry with oblique incidence creates a chiral response. In contrast, exploiting the third dimension with two rotated antennas allows for intrinsic chiral structures where the structure itself lacks mirror symmetry. The dual-layer structure gives access to intrinsic chirality induced within the meta-structures independent of the angle of incidence. For this purpose, again two rotated antennas in both layers are simulated. The geometric parameters of both antennas are the same, but the antenna in the lower layer is

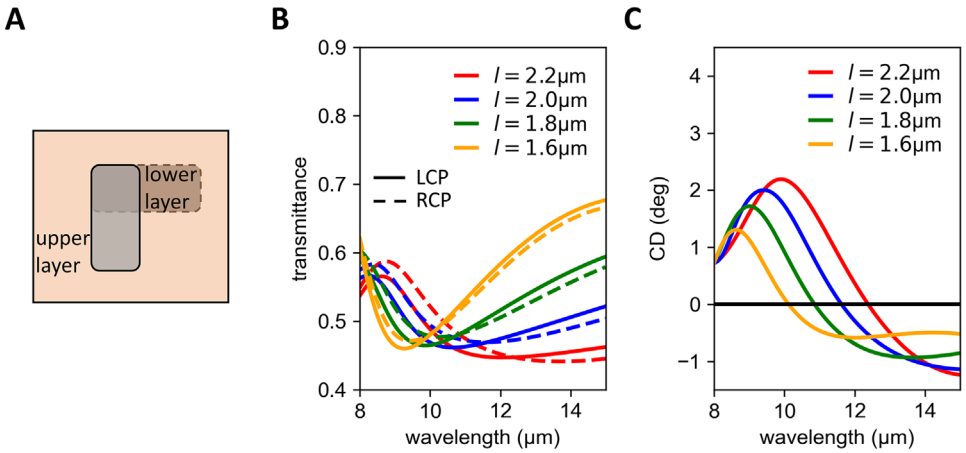

Figure 6. Simulations for possible applications. A) Schematic sketch of the IST antenna arrangement in both layers. Rotating the antennas with respect to each other results in an intrinsic chiral metasurface. B) Simulated transmittance for antenna with varied lengths for left (solid) and right (dashed) circularly polarized light. C) Calculated circular dichroism (CD) from the simulated spectra in (B). Tuning the antenna lengths leads to a shift in the maximum CD values toward larger wavelengths.

rotated by 90° (see schematic sketch in **Figure** 6A). The width of both antennas is set to 0.8 μm, and the length is varied. The simulated transmittance spectra T for various antenna lengths and left-handed circularly polarized (LCP) and right-handed circularly polarized (RCP) light are shown in Figure 6B. The observed resonance shifts upon increasing the antenna lengths toward larger wavelengths. Moreover, the two different polarizations are transmitted differently, indicating the chiral response of the sample employed. Next, the circular dichroism (CD) is calculated according to equation[31,55]

$$CD = 33\left(\log\left(T_{RCP}\right) - \log\left(T_{LCP}\right)\right) \quad (1)$$

The CD spectra obtained are shown in Figure 6C. The CD response of the antennas shifts for increased antenna lengths toward larger wavelengths.

The CD values are comparable to already demonstrated values in literature for example by Yin et al. for metallic antennas embedded in the dielectric PCM $Ge_3Sb_2Te_6$ where the CD ≈4 degrees was tuned by the refractive index change caused by crystallization of the PCM.[31]

Notice that the experimental demonstration of these chiral structures is not limited by the fabrication, but by the availability of broadband circularly polarized light in that spectral range in our lab. The CD values can be further increased by optimizing the sample with regard to the thickness of the spacer layer to increase the coupling strength of the nanorod antennas and achieving more pronounced resonance modes with tailored rod antenna aspect ratio. This is not within the scope of the current manuscript and will be demonstrated in a future publication.

3. Discussion

In summary, we have demonstrated a new fabrication approach of optically writing antenna structures within a dual-layer IST metasurface separated by a thin germanium layer. These antennas are programmed by switching the PCM from above and below and applying subsequent reamorphization spots to the upper layer. Careful design of the dielectric spacing layer with particular interest in the thermal properties, e.g. with additional Multiphysics simulations, could allow for fully disentangled response of the different IST layers circumventing the additional erasing step.

Individual control over both layers is shown by creating antenna arrays with varied antenna lengths. Moreover, two antenna arrays in both layers rotated with respect to each other enable polarization dependent resonances. The fabrication process of directly programming antenna structures with laser irradiation replaces cumbersome fabrication techniques such as electron lithography, especially beneficial for multi-layer structures which require several masks and processing steps.

Moreover, we anticipate that our concept can be directly transferred to intrinsic chiral metasurfaces introducing a novel concept of tuning the chirality of the system by reconfiguring the shapes of the antennas, which promises enhanced sensing of chiral molecules.[10,31,56]

Within the realm of cascaded metasurfaces, e.g. for information encoding or secret sharing holography,[8] aligning different metasurfaces displays a crucial disadvantage which can be solved by optically programming the dual-layer metasurfaces within only a few fabrication steps in one layerstack. Consequently, we envision that optically programmed cascaded IST dual-layer metasurfaces allow for aberration corrections[57] inherently limiting metasurfaces in real-world environments. Moreover, dual-layer metasurfaces could improve computer vision capabilities for thermal imaging via optical preprocessing, for example low-level feature extraction such as edge detection operating in the infrared spectral range.[58,59]

4. Experimental Section

Sample Fabrication: Direct current magnetron sputtering was used to deposit a 50 nm thin amorphous In_3SbTe_2 film on top of 1 × 1 cm^2 infrared transparent CaF_2 substrate, followed by a 100 nm thin germanium layer. Afterward, again 50 nm of amorphous IST was sputtered, and a 70 nm thin

$ZnS:SiO_2$ capping layer to protect the PCM from dust and oxidization. A constant argon flow of 20 sccm was chosen. The PCM sputtering was done in constant power mode with 23 W and a deposition rate of 0.09 nm s^{-1}. The germanium layer (capping layer) was fabricated with 20 W (60 W) and a rate of 0.05 nm s^{-1} (0.03 nm s^{-1}).

Optical Switching: Optical crystallization of the IST layer was achieved with a home-build laser setup. Here, a laser diode with 660 nm wavelength is focused by a 10x objective and NA = 0.25 onto the sample. Precise movements of the sample were achieved with a Thorlabs closed-loop piezo controller (BCP303) and coarse movements with Thorlabs NanoMax-TS stepper motors. An external pulse generator (Keysight 3320A) controls the number of individual laser pulses in one spot.

The optical writing of antennas in the upper layer was done by crystallizing the sample from above, while the optical writing of antennas in the lower layer was achieved by crystallizing both layers through the substrate with a subsequent erasing step of the antennas in the upper layer from above. The alignment is solely done optically using a live view image of a camera. Since the size of the optically written antennas was in the range of several micrometers, the antennas could be precisely aligned with uncertainties in the range of a few hundred nanometers.

To image the fabricated antenna arrays in the upper, reflectance light microscopy was utilized with moderate intensity. The low transmittance of the germanium layer ensures that only the antennas in the upper layer are recorded. In contrast, to image antennas in the lower layer, transmittance light microscopy was employed with maximum illumination intensity to exploit the remaining transmittance through the germanium layer.

FTIR Measurements: The measured transmittance spectra were recorded with a Bruker Vertex 70 interferometer connected to a Hyperion 2000 microscope. Accordingly, a 15x Cassegrain objective with an angular range from 10° to 24° was employed for measuring specific antenna arrays and for collecting the light after passing the sample. Each antenna array had a size of 16.5 × 16.5 μm^2 and consisted of 5 × 5 antennas in x- and y-direction. Knife edge apertures and an infrared polarizer were used in all measurements. Each measurement was recorded with 2000 scans and a spectral resolution of 8 cm^{-1}, referenced to an area without any antennas.

Simulations: Numerical infrared transmittance simulations were performed with the commercially available program CST Studio Suite from Dassault Systems. As excitation, Floquet Mode Ports have been chosen with periodic boundaries in lateral dimensions. The permittivity of IST was modeled according to experimental values,[36] while for CaF_2, the $ZnS:SiO_2$ capping layer and germanium a constant refractive index of 1.4, 2.1, and 4.17 have been chosen. The thermal Multiphysics simulations were executed with CST Studio Suite as well with open boundary conditions. Here, a gaussian laser beam with a power of 25 mW for illuminating the sample from the top, and 50 mW power for illuminating the sample from below was employed. In the experiment, 21 subsequent laser pulses were applied to achieve crystallization. To take this in the simulation into account, the simulated laser power was increased accordingly. The material parameters (permittivity at 660 nm, thermal conductivity, and specific heat capacity) for thermal simulations were chosen for CaF_2 (1.2, 9.71 W/(K m) and 854 J/(K kg)), for germanium (4.3 + 26.7i, 64 W/(K m) and 322 J/(K kg)), for amorphous IST (15 + 13.7i, 7.65 W/(K m) and 229 J/(K kg)), for the capping (5.1 + 0.44i, 0.5 W/(K m) and 530 J/(K kg)), for SiO_2 (2.14 + 0.005i, 1.3 W/(K m) and 680 J/(K kg)) and for air (1, 0.026 W/(K m) and 1005 J/(K kg)).

Supporting Information

Supporting Information is available from the Wiley Online Library or from the author.

Acknowledgements

The authors acknowledge support by the Deutsche Forschungsgemeinschaft (DFG No. 518913417 & SFB 917 "Nanoswitches").

Open access funding enabled and organized by Projekt DEAL.

Conflict of Interest

The authors declare no conflict of interest.

Author Contributions

L.C. and T.T. conceived the research idea; L.C. and M.K. designed the research, carried out the optical switching, and performed measurements and simulations. L.J. performed SNOM measurements; S.M. and D.N.C. carried out the temperature simulations. M.W. provided the sputtering equipment and phase-change material expertise; all authors contributed to writing the manuscript.

Data Availability Statement

The data that support the findings of this study are available from the corresponding author upon reasonable request.

Keywords

active, chirality, metasurface, multi-layer, optical programming

Received: January 20, 2025
Revised: March 10, 2025
Published online: April 7, 2025

[1] N. Yu, F. Capasso, *Nat. Mater.* **2014**, *13*, 139.
[2] S. Wang, P. C. Wu, V.-C. Su, Y.-C. Lai, M.-K. Chen, H. Y. Kuo, B. H. Chen, Y. H. Chen, T.-T. Huang, J.-H. Wang, R.-M. Lin, C.-H. Kuan, T. Li, Z. Wang, S. Zhu, D. P. Tsai, *Nat. Nanotechnol.* **2018**, *13*, 227.
[3] N. Yu, P. Genevet, M. A. Kats, F. Aieta, J.-P. Tetienne, F. Capasso, Z. Gaburro, *Science* **2011**, *334*, 333.
[4] C.-S. Park, V. R. Shrestha, W. Yue, S. Gao, S.-S. Lee, E.-S. Kim, D.-Y. Choi, *Sci. Rep.* **2017**, *7*, 2556.
[5] G. Zheng, H. Mühlenbernd, M. Kenney, G. Li, T. Zentgraf, S. Zhang, *Nat. Nanotechnol.* **2015**, *10*, 308.
[6] A. I. Kuznetsov, M. L. Brongersma, J. Yao, M. K. Chen, U. Levy, D. P. Tsai, N. I. Zheludev, A. Faraon, A. Arbabi, N. Yu, D. Chanda, K. B. Crozier, A. V. Kildishev, H. Wang, J. K. W. Yang, J. G. Valentine, P. Genevet, J. A. Fan, O. D. Miller, A. Majumdar, J. E. Fröch, D. Brady, F. Heide, A. Veeraraghavan, N. Engheta, A. Alù, A. Polman, H. A. Atwater, P. Thureja, R. Paniagua-Dominguez, et al., *ACS Photonics* **2024**, *11*, 816.
[7] F. Mei, G. Qu, X. Sha, J. Han, M. Yu, H. Li, Q. Chen, Z. Ji, J. Ni, C.-W. Qiu, Q. Song, Y. Kivshar, S. Xiao, *Nat. Commun.* **2023**, *14*, 6410.
[8] P. Georgi, Q. Wei, B. Sain, C. Schlickriede, Y. Wang, L. Huang, T. Zentgraf, *Sci. Adv. 7*, abf9718.
[9] L. Zhang, L. Zhang, R. Xie, Y. Ni, X. Wu, Y. Yang, F. Xing, X. Zhao, Z. You, *Adv. Sci.* **2023**, *10*, 2300542.
[10] H. S. Khaliq, A. Nauman, J.-W. Lee, H.-R. Kim, *Adv. Opt. Mater.* **2023**, *11*, 2300644.
[11] M. Hentschel, M. Schäferling, X. Duan, H. Giessen, N. Liu, *Sci. Adv. 3*, 1602735.
[12] M. Hentschel, M. Schäferling, T. Weiss, N. Liu, H. Giessen, *Nano Lett.* **2012**, *12*, 2542.
[13] M. Choi, A. Alù, A. Majumdar, *Observation of Photonic Chiral Flatbands arXiv:2408.09328*, **2024**, https://arxiv.org/abs/2408.09328.
[14] Y. Zhao, A. N. Askarpour, L. Sun, J. Shi, X. Li, A. Alù, *Nat. Commun.* **2017**, *8*, 14180.
[15] J. T. Collins, D. C. Hooper, A. G. Mark, C. Kuppe, V. K. Valev, *ACS Nano* **2018**, *12*, 5445.

[16] P. Chen, Z.-X. Shen, C.-T. Xu, Y.-H. Zhang, S.-J. Ge, L.-L. Ma, W. Hu, Y.-Q. Lu, *Laser Photonics Rev.* **2022**, *16*, 2200011.
[17] M. Wuttig, H. Bhaskaran, T. Taubner, *Nat. Photonics* **2017**, *11*, 465.
[18] M. Wuttig, N. Yamada, *Nat. Mater.* **2007**, *6*, 824.
[19] M. Wuttig, V. L. Deringer, X. Gonze, C. Bichara, J.-Y. Raty, *Adv. Mater.* **2018**, *30*, 1803777.
[20] M. Wuttig, C.-F. Schön, J. Lötfering, P. Golub, C. Gatti, J.-Y. Raty, *Adv. Mater.* **2023**, *35*, 2208485.
[21] B. J. Kooi, M. Wuttig, *Adv. Mater.* **2020**, *32*, 1908302.
[22] L. Guarneri, S. Jakobs, A. von Hoegen, S. Maier, M. Xu, M. Zhu, S. Wahl, C. Teichrib, Y. Zhou, O. Cojocaru-Mirédin, M. Raghuwanshi, C.-F. Schön, M. Drögeler, C. Stampfer, R. P. S. M. Lobo, A. Piarristeguy, A. Pradel, J.-Y. Raty, M. Wuttig, *Adv. Mater.* **2021**, *33*, 2102356.
[23] O. Cojocaru-Mirédin, Y. Yu, J. Köttgen, T. Ghosh, C.-F. Schön, S. Han, C. Zhou, M. Zhu, M. Wuttig, *Adv. Mater.* **2024**, *36*, 2403046.
[24] Q. Wang, E. T. F. Rogers, B. Gholipour, C.-M. Wang, G. Yuan, J. Teng, N. I. Zheludev, *Nat. Photonics* **2016**, *10*, 60.
[25] A. Tittl, A.-K. U. Michel, M. Schäferling, X. Yin, B. Gholipour, L. Cui, M. Wuttig, T. Taubner, F. Neubrech, H. Giessen, *Adv. Mater.* **2015**, *27*, 4597.
[26] Y. Zhang, C. Fowler, J. Liang, B. Azhar, M. Y. Shalaginov, S. Deckoff-Jones, S. An, J. B. Chou, C. M. Roberts, V. Liberman, M. Kang, C. Ríos, K. A. Richardson, C. Rivero-Baleine, T. Gu, H. Zhang, J. Hu, *Nat. Nanotechnol.* **2021**, *16*, 661.
[27] C. C. Popescu, K. Aryana, P. Garud, K. P. Dao, S. Vitale, V. Liberman, H.-B. Bae, T.-W. Lee, M. Kang, K. A. Richardson, M. Julian, C. A. R. Ocampo, Y. Zhang, T. Gu, J. Hu, H. J. Kim, *Adv. Mater.* **2024**, *36*, 2400627.
[28] X. Yin, T. Steinle, L. Huang, T. Taubner, M. Wuttig, T. Zentgraf, H. Giessen, *Light: Sci. Appl.* **2017**, *6*, 17016.
[29] C. R. de Galarreta, A. M. Alexeev, Y.-Y. Au, M. Lopez-Garcia, M. Klemm, M. Cryan, J. Bertolotti, C. D. Wright, *Adv. Funct. Mater.* **2018**, *28*, 1704993.
[30] Z. Fang, R. Chen, J. E. Fröch, Q. A. A. Tanguy, A. I. Khan, X. Wu, V. Tara, A. Manna, D. Sharp, C. Munley, F. Miller, Y. Zhao, S. Geiger, K. F. Böhringer, M. S. Reynolds, E. Pop, A. Majumdar, *ACS Nano* **2024**, *18*, 11245.
[31] X. Yin, M. Schäferling, A.-K. U. Michel, A. Tittl, M. Wuttig, T. Taubner, H. Giessen, *Nano Lett.* **2015**, *15*, 4255.
[32] X. Sha, K. Du, Y. Zeng, F. Lai, J. Yin, H. Zhang, B. Song, J. Han, S. Xiao, Y. Kivshar, Q. Song, *Sci. Adv. 10*, adn9017.
[33] L. Conrads, A. Heßler, K. G. Wirth, S. Meyer, M. Wuttig, D. N. Chigrin, T. Taubner, *Adv. Opt. Mater.* **2023**, *11*, 2300499.
[34] A. Leitis, A. Heßler, S. Wahl, M. Wuttig, T. Taubner, A. Tittl, H. Altug, *Adv. Funct. Mater.* **2020**, *30*, 1910259.
[35] Y. Maeda, H. Andoh, I. Ikuta, H. Minemura, *J. Appl. Phys.* **1988**, *64*, 1715.
[36] A. Heßler, S. Wahl, T. Leuteritz, A. Antonopoulos, C. Stergianou, C.-F. Schön, L. Naumann, N. Eicker, M. Lewin, T. W. W. Maß, M. Wuttig, S. Linden, T. Taubner, *Nat. Commun.* **2021**, *12*, 924.
[37] A. Heßler, S. Wahl, P. T. Kristensen, M. Wuttig, K. Busch, T. Taubner, *Nanophotonics* **2022**, *11*, 3871.
[38] A. Heßler, L. Conrads, K. G. Wirth, M. Wuttig, T. Taubner, *ACS Photonics* **2022**, *9*, 1821.
[39] L. Conrads, A. Heßler, L. Völkel, K. Wilden, A. Strauch, J. Pries, M. Wuttig, T. Taubner, *ACS Nano* **2023**, *17*, 25721.
[40] L. Conrads, N. Honné, A. Ulm, A. Heßler, R. Schmitt, M. Wuttig, T. Taubner, *Adv. Opt. Mater.* **2023**, *11*, 2202696.
[41] C. Meng, Y. Zeng, D. Lu, H. Zou, J. Wang, Q. He, X. Yang, M. Xu, X. Miao, X. Zhang, P. Li, *Nanoscale* **2023**, *15*, 6306.
[42] M. Giteau, L. Conrads, A. Mathwieser, R. Schmitt, M. Wuttig, T. Taubner, G. T. Papadakis, *Laser Photonics Rev.* **2025**, *19*, 2401438.
[43] L. Conrads, L. Schüler, K. G. Wirth, M. Wuttig, T. Taubner, *Nat. Commun.* **2024**, *15*, 3472.
[44] D. Lu, Y. Zeng, Q. Yan, Q. Chen, W. Ma, X. Luo, M. Xu, X. Yang, P. Li, *Nanophotonics* **2024**, *13*, 937.
[45] L. Conrads, L. Schüler, K. G. Wirth, A. Cleri, A. Heßler, L. Jung, M. Wuttig, D. Chigrin, J.-P. Maria, T. Taubner, *Sci. Adv.* **2025**,*11*, adr6844.
[46] L. Conrads, F. Bontke, A. Mathwieser, P. Buske, M. Wuttig, R. Schmitt, C. Holly, T. Taubner, *Infrared Beam-shaping on Demand via Tailored Geometric Phase Metasurfaces employing the Plasmonic Phase-Change Material, In3SbTe2, arXiv:2408.05044*, **2024**, https://arxiv.org/abs/2408.05044.
[47] T. Amotchkina, M. Trubetskov, D. Hahner, V. Pervak, *Appl. Opt.* **2020**, *59*, A40.
[48] S. Meyer, Z. Y. Tan, D. N. Chigrin, *Nanophotonics* **2020**, *9*, 675.
[49] F. Miller, R. Chen, J. E. Fröch, H. Rarick, S. Geiger, A. Majumdar, *Opt. Lett.* **2023**, *48*, 2385.
[50] N. Liu, H. Giessen, *Angew. Chem., Int. Ed.* **2010**, *49*, 9838.
[51] R. Hillenbrand, T. Taubner, F. Keilmann, *Nature* **2002**, *418*, 159.
[52] M. Lewin, B. Hauer, M. Bornhöfft, L. Jung, J. Benke, A.-K. U. Michel, J. Mayer, M. Wuttig, T. Taubner, *Appl. Phys. Lett.* **2015**, *107*, 151902.
[53] T. Taubner, F. Keilmann, R. Hillenbrand, *Opt. Express* **2005**, *13*, 8893.
[54] T. W. W. Maß, Concepts for Improving Surface-Enhanced Infrared Spectroscopy, Dissertation RWTH Aachen University **2018**.
[55] R. W. Woody, *Methods in Enzymology*, *246*, Elsevier, Amsterdam, The Netherlands **1995**, pp. 34–71.
[56] A. Lininger, G. Palermo, A. Guglielmelli, G. Nicoletta, M. Goel, M. Hinczewski, G. Strangi, *Adv. Mater.* **2023**, *35*, 2107325.
[57] A. McClung, M. Mansouree, A. Arbabi, *Light: Sci. Appl.* **2020**, *9*, 93.
[58] M. Cotrufo, S. Singh, A. Arora, A. Majewski, A. Alù, *Optica* **2023**, *10*, 1331.
[59] B. T. Swartz, H. Zheng, G. T. Forcherio, J. Valentine, *Sci. Adv.* **2024**, *10*, adk0024.